On the identifiability of Hill-1948 plasticity model with a single biaxial test on very thin sheet

Morgan Bertin, François Hild, Stéphane Roux

STRAIN - Manuscript Submission

On the identifiability of Hill-1948 plasticity model with a single biaxial test on very thin sheet

Morgan Bertin, François Hild[1] and Stéphane Roux

LMT (ENS Paris-Saclay, CNRS, Université Paris-Saclay)

61 avenue du Président Wilson, 94235 Cachan cedex, France

[1]Corresponding author. Email: hild@lmt.ens-cachan.fr

ABSTRACT: One biaxial experiment is performed on an ultra-thin specimen made of 17-7 precipitation hardened stainless steel. An anti-wrinkling setup allows for the characterization of the mechanical behavior with Integrated Digital Image Correlation (IDIC). A sensitivity analysis assesses the amount of data available but reveals a discrepancy between observation and model that is interpreted as the occurrence of wrinkling in a confined boundary layer. From this observation, the identification is performed on a refined region of interest where reliable data are accessible. The calibration of parameters of various constitutive equations is performed. In particular, the identifiability of the so-called Hill-1948 model is analyzed.

KEY WORDS: Anisotropy, Digital Image Correlation (DIC), Full field measurements, Plasticity

Introduction

For engineering design purposes, Tresca [35] or von Mises [36] isotropic yield criteria are commonly used and generally give satisfactory results. However, isotropic plasticity of formed materials is not common and anisotropy is the rule rather than the exception. Consequently sheet metal anisotropy is a key issue to improve manufacturing processes and mechanical designs. Lankford et al. [19] proposed an experimental ratio to characterize plastic anisotropy. Hill [15] and Dorn [11] works have led to the first models of anisotropic plastic flow. Their developments have been extended to describe more complex behavior [16].

There are different experimental techniques for calibrating constitutive laws of metallic materials [17]. Among them cruciform samples have been considered. The first set of works has dealt with geometries for which the stress state is made as uniform as possible in the central part [10, 8, 18, 38, 26]. Such geometries were validated experimentally [13]. Their main advantage lies in the fact that strains and stresses are concentrated and virtually uniform in the gauge section. When samples are very thin, this route is difficult to follow since it implies even thinner gauge sections.

The second route consists of performing biaxial experiments on cruciform samples with no thickness variations. Consequently, the stress and strain fields are heterogeneous everywhere and inverse identification techniques have to be used [3] in conjunction with full-field displacement measurements (e.g., via Digital Image Correlation [33]). Finite Element Model Updating was performed to calibrate anisotropic plasticity parameters [21, 34, 29]. It was also shown that Integrated Digital Image Correlation could be used to tune von Mises plasticity parameters [5] on such type of samples. This technique will be used herein to investigate plastic anisotropy.

The present study aims for the calibration of the so-called Hill-1948 model [15, 2]. The latter is one of the standard and most widely used model in nowadays commercial finite element codes [30]. Integrated-DIC will be utilized. It allows displacement fields and material parameters to be measured in only one single step [14, 20]. Elastoplasticity was also analyzed within such a framework [25]. Réthoré [28] showed that such technique was particularly robust for the identification of a damage model. In the present work, a single experiment on an ultra-thin biaxial specimen is performed and four constitutive laws with increasing complexity are considered to challenge the sought behavior. To enhance the relevance of the model, all data (i.e., displacement fields and reaction forces) are equitably weighted via a Bayesian foundation [25, 5, 4].

The paper is divided into two main sections. First,

the chosen constitutive models are introduced and the integrated-DIC identification methodology is recalled. The interested reader will find additional details in Ref. [5]. Second, the biaxial experiment is presented in which an anti-wrinkling device aims to prevent the out-of-plane motions of the ultra-thin specimen. The identifiability of the chosen anisotropic plasticity model is finally assessed in a two-step procedure.

Theoretical and methodological framework

Investigated constitutive laws

Four constitutive laws are investigated, namely, (A) linear and isotropic elasticity (with Young's modulus E and Poisson's ratio ν), (B) linear kinematic hardening with von Mises flow rule, (C) exponential kinematic hardening with von Mises flow rule, and (D) linear kinematic hardening with quadratic yield criterion (i.e., the so-called Hill-1948 model [15, 2]). The total strain rate $\dot{\boldsymbol{\epsilon}}$ is written in terms of elastic and plastic strain rates $\dot{\boldsymbol{\epsilon}} = \dot{\boldsymbol{\epsilon}}_{el} + \dot{\boldsymbol{\epsilon}}_{pl}$ where $\dot{\boldsymbol{\epsilon}}_{el}$ is the elastic strain rate tensor and $\dot{\boldsymbol{\epsilon}}_{pl}$ the plastic strain rate tensor. The yield surface $J_2(\boldsymbol{\sigma} - \boldsymbol{X}) = \sigma_y$ is defined such that J_2 is the second invariant of the stress deviator tensor, $\boldsymbol{X}$ the back-stress, and σ_y the yield stress. As a first approximation, a linear kinematic hardening model is chosen for the back-stress rate [27]

$$\dot{\boldsymbol{X}} = \frac{2}{3} C \dot{\boldsymbol{\epsilon}}_{pl} \tag{1}$$

where C is the hardening modulus. Under the assumption of exponential kinematic hardening, the back-stress becomes [12, 22]

$$\dot{\boldsymbol{X}} = \frac{2}{3} C \dot{\boldsymbol{\epsilon}}_{pl} - c \boldsymbol{X} \dot{p} \tag{2}$$

where C and c are material parameters, p the cumulative plastic strain. Last, the quadratic anisotropic yield criterion [15] is associated with the linear kinematic hardening law (B). The latter criterion is an extension of the von Mises criterion, and can be expressed in terms of rectangular Cartesian stress components as

$$\begin{aligned} f^2(\boldsymbol{\sigma}) &= H_1(\sigma_{22} - \sigma_{33})^2 + H_2(\sigma_{33} - \sigma_{11})^2 \\ &+ H_3(\sigma_{11} - \sigma_{22})^2 + 2H_4\sigma_{23}^2 \\ &+ 2H_5\sigma_{31}^2 + 2H_6\sigma_{12}^2 \end{aligned} \tag{3}$$

where H_i are constants expressed with the normal yield stress ratio ($R_{11} = \bar{\sigma}_{11}/\sigma_y$, $R_{22} = \bar{\sigma}_{22}/\sigma_y$, $R_{33} = \bar{\sigma}_{33}/\sigma_y$) and those in shear ($R_{12} = \sqrt{3}\bar{\sigma}_{12}/\sigma_y$, $R_{23} = \sqrt{3}\bar{\sigma}_{23}/\sigma_y$, $R_{31} = \sqrt{3}\bar{\sigma}_{31}/\sigma_y$) both with respect to the axes of anisotropy

$$\begin{aligned} H_1 &= \frac{1}{2}\left(\frac{1}{R_{22}^2} + \frac{1}{R_{33}^2} - \frac{1}{R_{11}^2}\right), \quad H_4 = \frac{3}{2}\frac{1}{R_{23}^2} \\ H_2 &= \frac{1}{2}\left(\frac{1}{R_{33}^2} + \frac{1}{R_{11}^2} - \frac{1}{R_{22}^2}\right), \quad H_5 = \frac{3}{2}\frac{1}{R_{31}^2}, \\ H_3 &= \frac{1}{2}\left(\frac{1}{R_{11}^2} + \frac{1}{R_{22}^2} - \frac{1}{R_{33}^2}\right), \quad H_6 = \frac{3}{2}\frac{1}{R_{12}^2} \end{aligned}$$

The computation being two dimensional (i.e., plane stress), R_{31} and R_{23} are insensitive and set to 1 hereafter (and hence $H_4 = H_5 = 3/2$). One of the three parameters H_1, H_2, and H_3 must be chosen to decorrelate its value from the yield stress and hence $H_1 = 1/2$ is chosen. Therefore, only three additional material parameters, i.e., H_2, H_3, and H_6, remain to be determined.

Integrated-DIC

There are different approaches to DIC. The first one consists of registering a series of independent zones of interest [33]. Nowadays, such approach is called local DIC. It will not be used herein. Global DIC is based upon continuity requirements over the whole region of interest [37]. One possible parameterization of the displacement fields is provided by finite element shape functions [7, 32, 6]. Such approaches can be made fully consistent with finite element simulations by implementing so-called integrated approaches [20, 28, 25, 5]. In the following, the identification of the material parameters will rely on Integrated DIC where the unknowns are no longer the displacement at each node but the sought parameters. It is based on global DIC [6] that consists of the registration of an image f in the reference configuration and a series of pictures g in the deformed configurations. Assuming gray level conservation, the registration problem consists of minimizing the sum of squared differences between the deformed image corrected by the measured displacement $\boldsymbol{u}(\boldsymbol{x}, t)$ and the reference image (written for each time t independently)

$$\chi_f^2 = \frac{1}{2\gamma_f^2 N_\Omega N_t} \sum_t \sum_\Omega (g(\boldsymbol{x} + \boldsymbol{u}(\boldsymbol{x}, t), t) - f(\boldsymbol{x}))^2 \tag{4}$$

with respect to the sought displacement fields $\boldsymbol{u}(\boldsymbol{x}, t)$, where $\boldsymbol{x}$ is any considered pixel. In this expression Ω denotes the Region of Interest (ROI), N_Ω its area in terms of the number of pixels it contains, and γ_f is the standard deviation (i.e., 2% of the dynamic range of f) of the white noise assumed to affect each image independently (including the reference one, which is responsible for the factor of $1/2$ coming as a multiplicative term in this functional). The load is also of importance for the identification because it increases the number of the measured quantities and as a consequence diminishes the relative uncertainty by enhancing the material parameters sensitivities [4]. Thus, a second objective function, χ_F^2, is introduced

$$\chi_F^2 = \frac{1}{N_F N_t \gamma_F^2} \{\boldsymbol{F}_m - \boldsymbol{F}_c\}^t \{\boldsymbol{F}_m - \boldsymbol{F}_c\} \tag{5}$$

where $\{\boldsymbol{F}_m\}$ are the measured reaction forces and $\{\boldsymbol{F}_c\}$ are the computed levels with respect to the chosen material parameter set, N_F the number of load cells for each actuator, N_t the number of steps and γ_F^2 the load variance. The identification based upon both observables, i.e., gray levels and reaction force, is achieved by minimizing the

global functional χ^2

$$\chi^2 = \frac{N_\Omega}{N_\Omega + N_F}\chi_f^2 + \frac{N_F}{N_\Omega + N_F}\chi_F^2 \qquad (6)$$

where the DIC and reaction force functionals have been introduced in Equations (4) and (5) respectively. The choice for the specific weight is issued from a Bayesian approach whereby the noise characteristics imposes the appropriate weights to be given to quadratic differences [4]. In particular, quadratic differences are to be evaluated with a metric equal to the inverse noise covariance.

In the following analyses, DIC measurements are based upon a global approach in which finite element discretizations are used to measure the displacement fields [6]. Meshes made of 3-noded triangles are considered. The displacement interpolation is linear within each element [20].

When using integrated-DIC, the displacement field $\boldsymbol{u}(\boldsymbol{x}, t, \{\boldsymbol{p}\})$ is parameterized with the sought material parameters $\{\boldsymbol{p}\}$ that become the generalized degrees of freedom. When a nonlinear behavior is investigated, the dependence of the displacement fields with the material parameters is nonlinear as well. Consequently, displacement fields, reaction forces and the corresponding sensitivities (i.e., first order derivatives of nodal displacements and reaction forces with respect to the sought parameters) are computed via finite element simulations. In the present case the commercial (implicit) finite element code used is Abaqus standard [2]. It is driven by the measured displacements on the boundary of the considered region of interest to compute the displacement fields and reaction forces.

A Gauss-Newton scheme is implemented to minimize the global functional by iteratively updating the material parameters. This type of minimization scheme requires the so-called Hessians to be computed (i.e., kinematic Hessian ($[\boldsymbol{M}]_{DIC}$) for global DIC, kinematic ($[\boldsymbol{M}]_{IDIC}$) and static ($[\boldsymbol{H}]_F$) Hessians to be combined to form the I-DIC Hessian ($[\boldsymbol{H}]_{IFDIC}$)). They correspond to the search directions of the minimization algorithm and their inverse is equal to the covariance matrix of the identified material parameters. The interested reader will find additional details on the implementation of such procedures in Ref. [5].

Analysis of biaxial experiment

This section investigates the mechanical behavior of a biaxial specimen, which is loaded with an electromechanical testing machine, mini-ASTREE [5] (Figure 1(a)). A triangular loading/unloading history is prescribed (Figure 1(b)) with load controlled mode. Prior to starting the experiment, 10 images and load measurements are acquired to assess the gray levels ($\gamma_f = 233$ gray levels) and load ($\gamma_F = 2.5$ N) uncertainties. 16-bit gray scale

images are acquired with a digital camera (pco.edge) associated with a telecentric lens (Figure 1(c)). The effective magnification is 12.5 μm per pixel or 80 pixels/mm. The gray level uncertainty is $\gamma_f = 233$ gray levels. Last, the load measurements and the image acquisitions are synchronized.

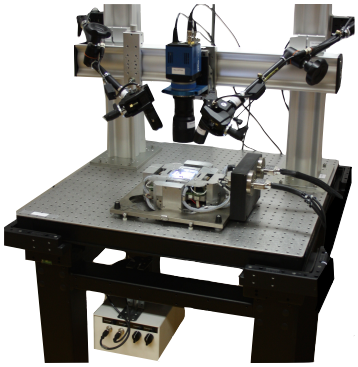

(a)

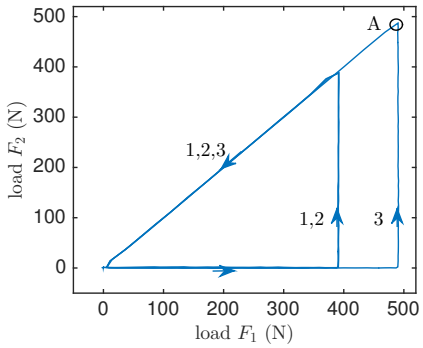

(b)

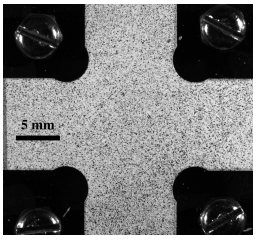

(c)

Figure 1: (a) Mini-ASTREE and its environment. (b) Prescribed loading history F_2 vs. F_1 consisting of successive triangles of increasing amplitudes. (c) Specimen and anti-wrinkling device (see the screws on the four corners)

The studied material is a precipitation hardened stainless steel (17-7 grade), which is treated in TH1050 condition (i.e., austenite conditioning, transformation and precipitation hardening [1]). The sample thickness is 50 μm where its initially guessed elastic properties and a standard yield stress originate from the steel manufacturer database [1]. Figure 2 shows an EBSD orientation map that reveals the material microstructure with the measured individual crystal orientations for the material in the investigated condition. The grains are small with an average size below 1 μm, which is more than 50 times smaller than the specimen thickness.

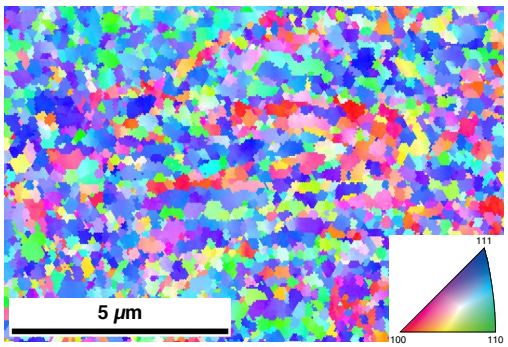

Figure 2: EBSD orientation map of the studied material in TH1050 condition [1]

The main experimental challenge concerns the specimen thickness that leads to wrinkling if no precautionary measures are taken. To maintain the surface flat in the center region (crucial to perform 2D-DIC analyses) an anti-wrinkling device is designed (see Figure 1(c)). It consists in holding the specimen between two plexiglas sheets maintained with four screws. The resulting pressure applied on the specimen is set as low as possible and aims to minimize the friction between the latter and the two plexiglass sheets. To perform DIC analyses a random speckle pattern is applied on the monitored surface. A post-experiment analysis has revealed that no marks have appeared on the plexiglass sheets and no paint loss was observed during the tests.

First identification: large ROI

Figure 3 shows the horizontal displacement field u_1 measured with global DIC associated with the three-noded triangular mesh with linear interpolation (T3) at the maximum loading amplitude (point A, see Figure 1(b)). The same mesh is used for DIC and most of the IDIC analyses.

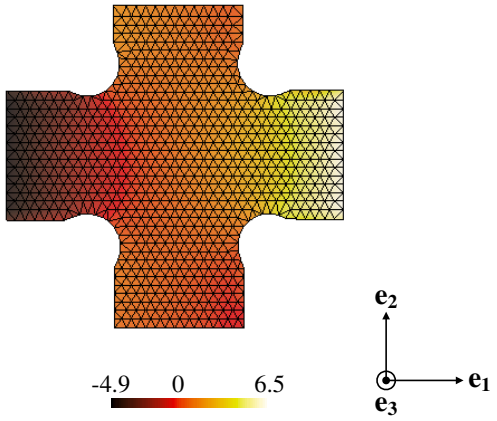

Figure 3: Horizontal displacement field u_1 at the maximum prescribed load amplitude corresponding to point A of the loading path of Figure 1(b). The displacements are expressed in pixels (1 pixel $\leftrightarrow$ 12.5 μm)

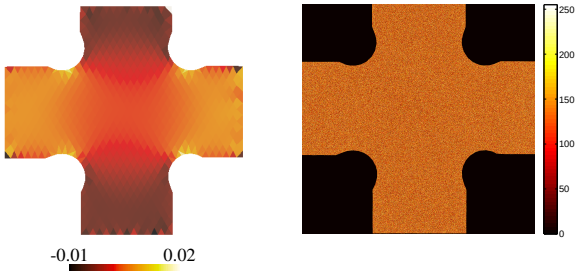

(a) (b)

Figure 4: (a) Strain field ϵ_{11}. (b) Residual map in gray levels at point A of the loading path (Figure 1(b)). The dynamic range of the pictures is 16 bits (Figure 1(c))

The maximum measured displacement is equal to 6.7 pixels corresponding to 83 μm. Figure 4 shows the strain field components ϵ_{11} and ϵ_{22} derived from the measured displacement field with DIC at point A of the loading path (Figure 1(b)). As expected the strains are concentrated near the four fillet radii and their amplitudes remain small with a largest value of 1.2 % in accordance with the sought objective, namely less than 1.5 %. However, numerous fluctuations are seen in the vicinity of the four arm edges. An investigation of the DIC residual map reveals that this trend does not originate from the DIC routine (Figure 4(c)). The second hypothesis is that the anti-wrinkling system is not perfect.

The identification is achieved by minimizing the global functional χ^2. A sensitivity analysis is performed for the Hill-1948 model (i.e., law D) as it possesses the largest number of material parameters. Their initial values are gathered in Table 1 and correspond to literature data [1, 23]. The analysis consists of the evaluation of the kinematic ($[\boldsymbol{M}]_{IDIC}$), static ($[\boldsymbol{H}]_F$), and global ($[\boldsymbol{H}]_{IFDIC}$) Hessians with an initial numerical analysis associated with the same mesh and the measured boundary conditions with DIC.

In a Gauss-Newton scheme, the Hessian corresponds to the matrix by which the parameter corrections are multiplied to decrease the right hand side residual vector. It is a square matrix whose columns and rows correspond to the set of sought parameters. In the present paper, the

meaning of each row and column can be understood by the material parameter indicated along the diagonal. It is worth noting that log-scales are used to improve the legibility of such type of representation. Consequently, absolute values are reported. Figure 5 shows the Hessians with a $\log_{10}$ scale. First, the kinematic Hessian ($[\boldsymbol{M}]_{IDIC}$) has more influence on the identification than the static Hessian ($[\boldsymbol{H}]_F$) because their largest eigenvalues are separated by more than 3 orders of magnitude and $[\boldsymbol{H}]_{IFDIC} \approx [\boldsymbol{M}]_{IDIC}$. Second, the hardening modulus C is insensitive for both kinematic and static Hessians. Conversely, the Poisson's ratio (ν) has the highest sensitivity followed by H_1, H_2, and H_3 that account for the anisotropic plastic behavior.

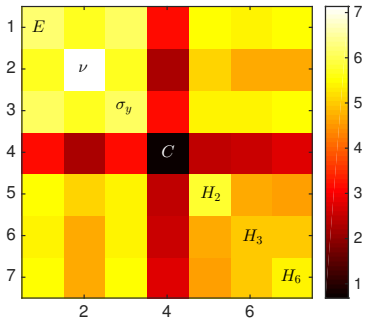

(a)

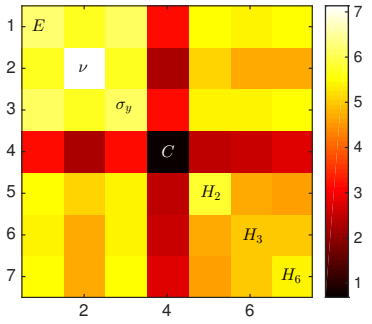

(b)

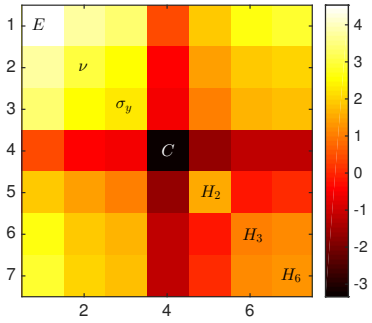

(c)

Figure 5: (a) Global ($[|\boldsymbol{H}_{IFDIC}|]$), (b) kinematic ($[|\boldsymbol{M}_{IDIC}|]$), and (c) static ($[|\boldsymbol{H}_F|]$) Hessians for Hill-1948 model. A $\log_{10}$ scale is used

The cross-correlation matrices associated with Hessians are constructed by normalizing each H_{ij} term of the Hessian by the square root of $H_{ii}H_{jj}$ (no index summation). The correlations between the parameters are depicted by such representation. Figure 6 shows that the Poisson's ratio has no correlation for the kinematic Hessian. Furthermore, the material parameters are more correlated to each other when looking at the static Hessian. In that case, the images are crucial for two reasons, namely, a greater sensitivity and less cross-correlations of the material parameters. To conclude on the sensitivity analysis, the behavior is mainly driven by an elastic behavior but small plastic strains occur near the four fillet radii. It is worth noting that the material parameters E and σ_y are correlated only based on kinematic data. The two parameters affect the initiation of the plastic strain by two means, $i)$ the higher the level of Young's modulus the sooner the plastic regime sets in, $ii)$ the lower the yield stress the sooner the plastic regime occurs as well.

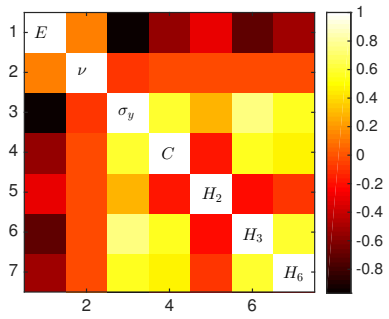

(a)

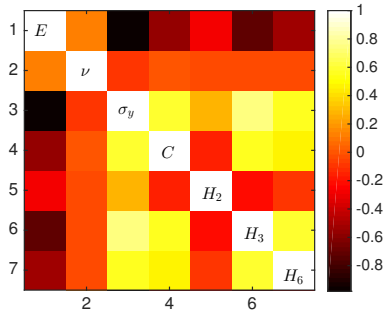

(b)

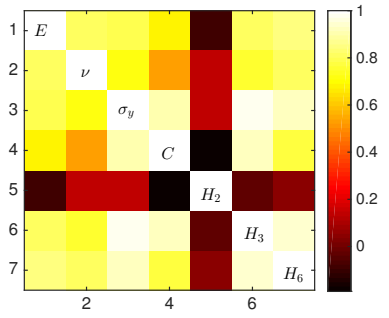

(c)

Figure 6: (a) Global, (b) kinematic, and (c) static cross-correlation matrices for Hill-1948 model

Figure 7 shows the sensitivity maps for all material parameters associated with Hill-1948 model at point A. First, the sensitivity map corresponding to the Poisson's ratio ν has the largest sensitive area. Second, even though plasticity is initially confined close to the fillet radii of the specimen, the sensitivity fields show that a significantly larger zone is concerned for identification purposes. Consequently, although not fully optimal [4], the present geometry is chosen for simplicity reasons. These results are in agreement with the previous conclusion and show that the present approach is a powerful tool to summarize a large quantity of data.

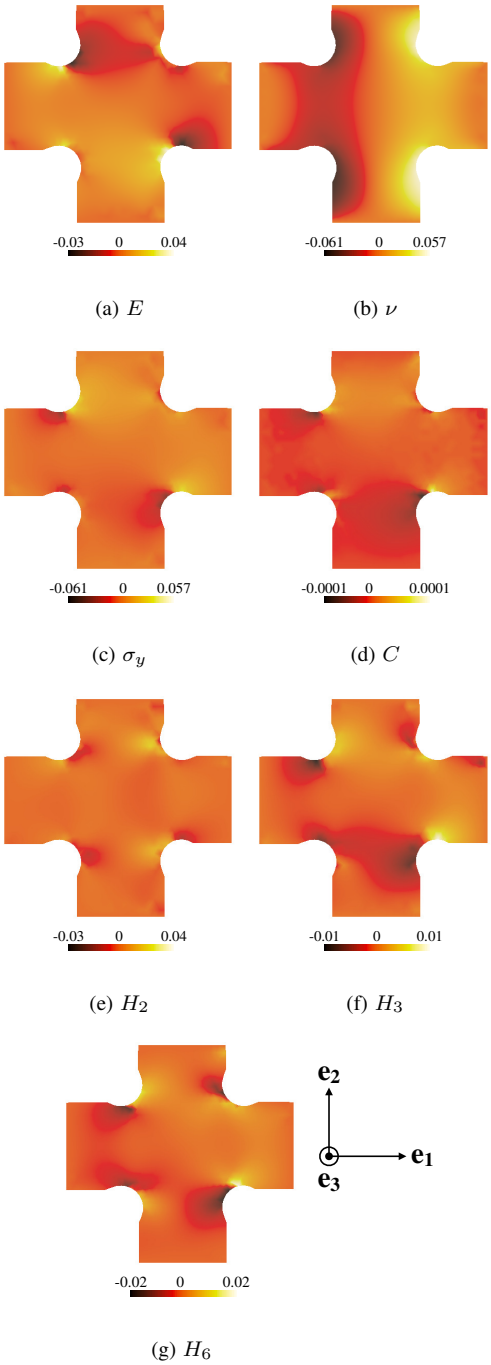

(a) E (b) ν

(c) σ_y (d) C

(e) H_2 (f) H_3

(g) H_6

Figure 7: Sensitivity fields for the parameters of Hill-1948 model for the component u_1 (in μm) for a 2% variation

The identification is performed with the four investigated laws and Figure 8 shows the registration residual history (χ_f) for DIC and IDIC. The DIC residuals are smaller than the IDIC residuals, which are almost identical for the four investigated laws. The fact that the residuals decrease during unloading phases originates from the quasi-elastic behavior. After unloading, the material recovers almost everywhere its original shape.

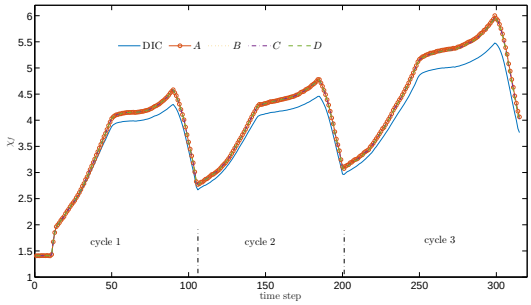

Figure 8: Global gray level residual history for DIC and for the four constitutive models investigated with IDIC

Table 1 gathers the assessed material parameters for the four constitutive laws. Their initial values ($\boldsymbol{p_0}$) are chosen according to literature data [1, 23]. The same Poisson's ratio value is obtained independently of the chosen constitutive model. The Young's modulus is affected when the model is elastoplastic. For the other material parameters, their values remain equivalent between the three elastoplastic models and the assessed anisotropic coefficients reveal an anisotropic plastic behavior. Regarding the residuals, the indicators χ and χ_f are equal and the load residual χ_F decreases as the constitutive model becomes more complex. Using an elastoplastic model improves by 25 % the load residual. However, it remains large in comparison to the noise level (i.e., 10 times higher). The change of global residual is small and there still is a model error. Last, the material parameters are different from the reference values, i) 10 % lower for the Young's modulus and ii) 10 % higher for the yield stress.

Table 1: Identified parameters (a) and identification residuals (b) via IDIC for the four laws over the entire loading history cycle of the biaxial test ("1^{st} — last" corresponds to the first and last value of the residuals)

law	E GPa	ν	σ_y MPa	C GPa	c	H_2	H_3	H_6
p_0	200	0.3	1300	10	10	0.5	0.5	1.5
A	200	0.33	—	—	—	—	—	—
B	173	0.33	1500	10	—	—	—	—
C	173	0.33	1500	10	10	—	—	—
D	166	0.33	1570	10	—	0.36	0.57	1.35

(a)

law	χ 1^{st} — last	χ_f 1^{st} — last	χ_F 1^{st} — last
p_0	3.61		
A	3.73—3.72	3.73—3.72	12.9—13.4
B	3.75—3.71	3.75—3.71	10.6—9.95
C	3.75—3.71	3.75—3.71	10.6—9.95
D	3.76—3.71	3.76—3.71	10.6—9.75

(b)

Figure 9 shows the measured and identified load histories for the four laws and for the two components F_1 and F_2. First, the loads do not return to zero as prescribed by the testing machine. Even if the assessed behavior leads to an accurate description of the loading phases, the model is unable to capture the unloading phases. This error explains why the load residuals are large with respect to the noise level. The latter may originate from the anti-wrinkling system that prevents the material to return to a perfect unloaded stage due to friction. However, qualitatively speaking, the biaxial trend is well captured by the elastoplastic models.

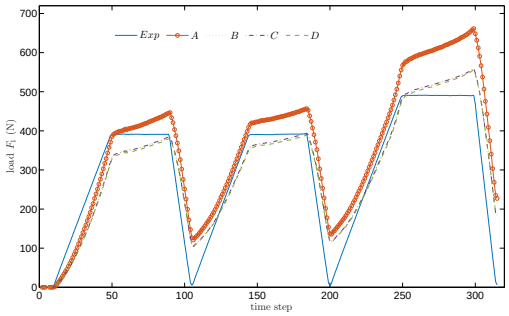

(a)

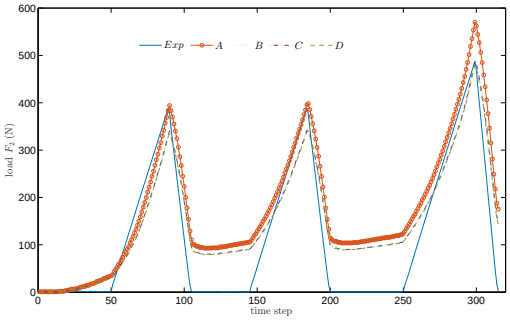

(b)

Figure 9: Measured and computed load histories of (a) F_1 and (b) F_2

Figure 10 shows the uniaxial stress/strain responses for laws B, C and D. Even though plastic anisotropy is

marked, the overall load response remains similar for the three models. This is due to the fact that plasticity is confined in the connecting radii since the maximum equivalent strain is less than 1.5 %. This level also explains why there is no observed gain in using nonlinear hardening (law C). Further, the Young's modulus is 4 % lower for model D in comparison with models B and C, which compensates for the higher yield stress ratio in the 90 ° direction (Figure 10).

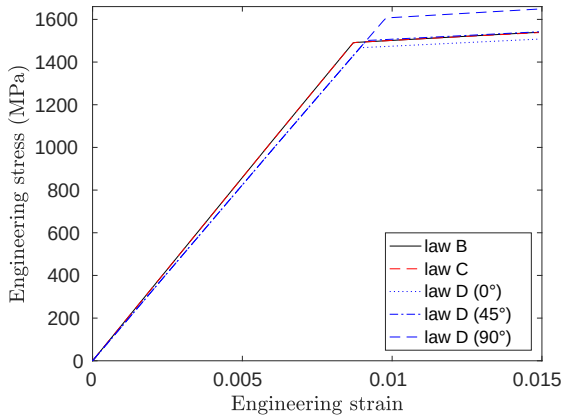

Figure 10: Uniaxial stress/strain responses for the three elastoplastic models

Figure 11 shows the horizontal component u_1 of the displacement field residual (difference between the IDIC and DIC displacement fields) at point A (Figure 1(b)). The highest differences are observed near the arm edges and the latter is stable and symmetrically distributed. It shows that the measured mechanical behavior does not correspond to the numerical solution. One possible explanation can be found in "line-tension theory," which is developed to account for easy wrinkling of thin elastic membranes under compression [31]. The edges of the arms that lie in the convex envelope of the free boundary can be shown to be totally screened, with zero stress tensor (and hence displaying a large propensity to wrinkle [9, 24]). Hence such regions, which precisely coincide with the support of the most salient displacement residuals, are not expected to be well described by the bulk constitutive law and the anti-wrinkling device cannot totally prevent such phenomena. However, after a redefinition of the effective free boundaries, the elastoplastic description should hold. To test this hypothesis, a second analysis is performed on a smaller ROI.

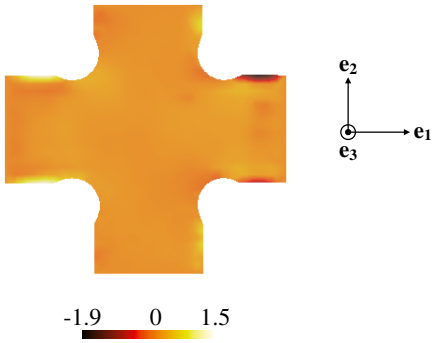

Figure 11: Horizontal component u_1 of the displacement residuals (IDIC-DIC) for Hill-1948 model (displacement differences are expressed in pixel, 1 pixel $\leftrightarrow$ 12.5 μm)

Second identification: smaller ROI

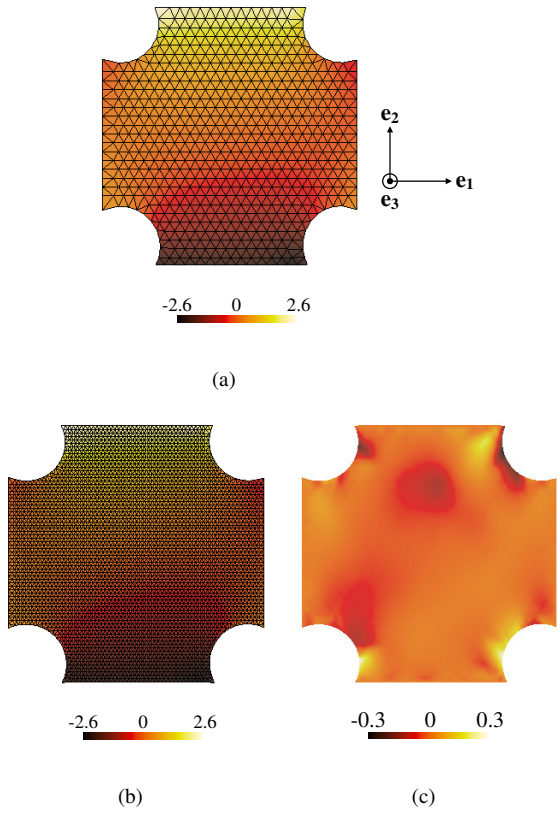

Figure 12: Displacement field component u_2 from (a) DIC, (b) IDIC with law D, and (c) corresponding displacement difference at point A of the loading path of Figure 1. The displacements are expressed in pixels (1 pixel $\leftrightarrow$ 12.5 μm)

A smaller ROI is investigated without the regions that are impacted by wrinkling. Figure 12 shows the component u_2 of the displacement field at point A (Figure 1(b)) for (a) DIC, (b) IDIC with law D, and (c) the displacement field residual between the two. The IDIC analysis uses a refined mesh to capture more precisely the elastoplastic behavior in the vicinity of the four fillet radii. The results show that the maximum value of the residual is smaller by more than one order of magnitude than the solution given by the larger ROI. This fact proves that the newly chosen region is less affected by wrinkles, which may prevent the identification of the material parameters.

Figure 13 shows the global Hessian ($[\boldsymbol{H}]_{IFDIC}$) and its cross-correlation matrix. The Poisson's ratio has no longer the largest level of sensitivity (see the results shown in Figure 5) but its influence is similar to the material parameters E, σ_y, and H_2. The smaller ROI cor-

responds to a smaller area that reduces the identifiability of the Poisson's ratio.

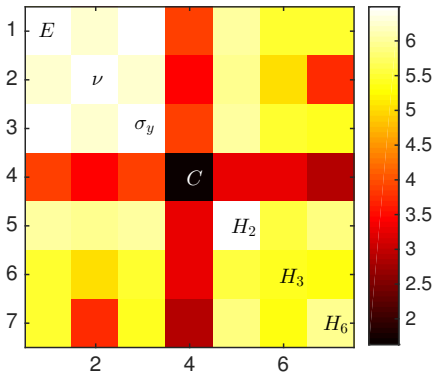

(a)

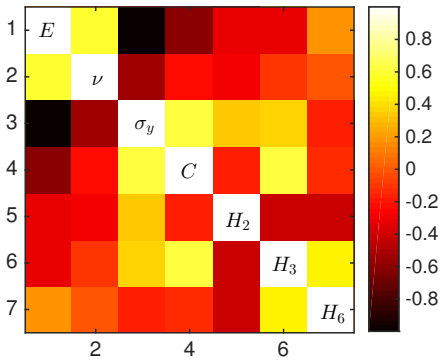

(b)

Figure 13: (a) Global Hessian ($[|\boldsymbol{H}_{IFDIC}|]$) in $\log_{10}$ scale and (b) its cross-correlation matrix

Table 2 gathers the assessed material parameters for the four constitutive laws. Different Poisson's ratio values are obtained for the four constitutive models. For the elastic model (law A), the Poisson's ratio increases because a "compromise" is made between the truly elastic behavior and plasticity where the deformation is essentially isochoric [5]. The Young's modulus is in better agreement with literature data [1, 23]. The residuals slightly decrease as the law complexity increases and are smaller by 30 % than those with the larger ROI. These results confirm that the anti-wrinkling device cannot totally prevent such phenomena from occurring.

To assess mesh sensitivity, Integrated DIC analyses are performed for Hill-1948 model (law D) with i) a refined mesh with an average element size 20 % smaller than the standard IDIC mesh size (D^*) and ii) a coarser mesh equal to the one used for DIC (D^{**}). No significant changes are observed in terms of global residuals. From the static residuals it is concluded that the intermediate mesh is the best even though all three mesh densities lead to equivalent global residuals.

Table 2: Identified parameters (a) and identification residuals via IDIC (b) for the four laws over the entire loading history cycle and the smaller ROI. D^* corresponds to the computation with a finer mesh and D^{**} to the DIC mesh

law	E GPa	ν	σ_y MPa	C GPa	c	H_2	H_3	H_6
p_0	200	0.3	1300	10	10	0.5	0.5	1.5
A	200	0.35	—	—	—	—	—	—
B	202	0.33	1300	10	—	—	—	—
C	202	0.33	1300	10	10	—	—	—
D	206	0.32	1260	10	—	0.44	0.5	1.35
D^*	206	0.32	1260	10	—	0.44	0.5	1.35
D^{**}	203	0.33	1280	10	—	0.45	0.5	1.40

(a)

law	χ 1^{st} — last	χ_f 1^{st} — last	χ_F 1^{st} — last
p_0	2.56		
A	2.71—2.70	2.71—2.70	11.6—12.7
B	2.69—2.68	2.69—2.68	10.2—10.8
C	2.69—2.68	2.69—2.68	10.2—10.8
D	2.69—2.68	2.69—2.68	10.2—10.5
D^*	2.69—2.68	2.69—2.68	10.2—10.4
D^{**}	2.69—2.68	2.69—2.68	10.2—10.6

(b)

Regarding the load residual (χ_F), the same improvement is reached with an elastoplastic law, but the newly chosen ROI does not improve their levels (i.e., 10 times the noise level). The results obtained for the refined ROI are closer than those obtained from the larger ROI. Figure 14 shows the sensitivity fields for Hill-1948 model (law D). Their main contribution is close to the fillet radii. Thus, the mesh size is of importance for identification purposes but a strong refinement (D^*) does not improve the identification quality, even as compared to the coarse mesh (D^{**}), as shown in Table 2. As already shown in Figure 7, the sensitivity fields act on a significantly larger zone than plasticity. This is due to the fact that stress redistributions are induced by the development of plasticity.

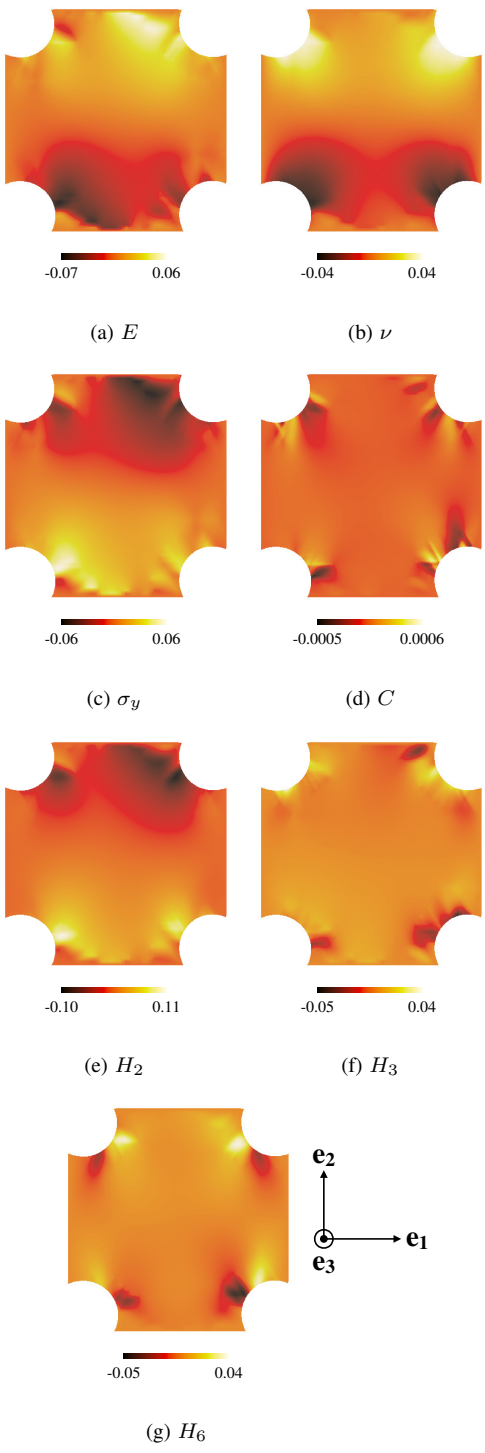

(a) E (b) ν

(c) σ_y (d) C

(e) H_2 (f) H_3

(g) H_6

Figure 14: Sensitivity fields for the parameters of Hill-1948 model and the component u_2 (μm)

Figure 15 shows the uniaxial stress/strain responses for laws B, C and D. Plastic anisotropy is less marked than in the previous case (Figure 10). Again, the use of linear kinematic hardening is sufficient in the present case since the maximum equivalent strain is less than 1.5 %. The Young's modulus difference between laws B, C and D is 2 %, which is very low. These levels remain close to an elastic postulate (law A) due to the confined nature of plasticity.

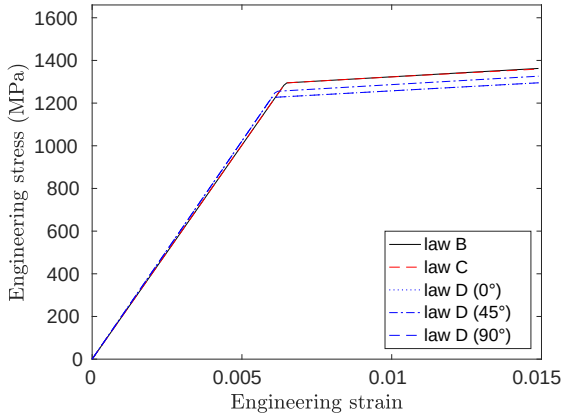

Figure 15: Uniaxial stress/strain responses for the three elastoplastic models

Conclusion

Four constitutive laws have been investigated with Integrated Digital Image Correlation to analyze a biaxial test on an ultra-thin sheet in precipitation hardened stainless steel. A dedicated anti-wrinkling system is designed

and employed to prevent non uniform out-of-plane displacements while loading and unloading the specimen. The calibration is performed over the entire loading history accounting for 3 loading/unloading cycles. The four laws lead to different residuals and the Hill-1948 model provides slightly better results. Thanks to full-field measurements, all the plane stress parameters that possess enough sensitivity could be calibrated with a unique test. Their validation via independent tests is one perspective to the present study.

The analysis of the experiment revealed that the specimen undergoes wrinkling on the connecting arms. The identification suffers from this effect as shown in the kinematic residual fields. To address this issue a smaller region of interest that focuses on the specimen center but considers the four fillet radii where plasticity occurs is chosen. The results show that this choice allows for a better identification since the elastoplastic behavior is less corrupted by experimental errors. Plastic anisotropy provides slightly better result but does not appear as necessary to predict the mechanical response of the investigated material.

This study shows that experiments on ultra-thin specimens may easily be affected by wrinkling. A full-field measurement technique, however, may expose one to meaningless identification. Thus, special care has to be exercised to avoid or minimize such effects, and residuals reveal very instrumental to detecting such difficulties. In the latter cases, the versatility of the integrated approach provides new pathways to tackle these problems.

Acknowledgments

The authors acknowledge the help of Dr. Hugo Leclerc in the implementation of the DIC codes. This work was supported by the RÃ©gion Ile de France (THERMOFLUIDE-RT project) and BPI France (DIC-CIT project).

References

1. AK-Steel. Mechanical characteristics 17-7 PH steel, 2013.
2. Abaqus Analysis. User's Manual, Version 2016. Dassault Systems, 2016.
3. S. Avril, M. Bonnet, A.-S. Bretelle, M. Grédiac, F. Hild, P. Ienny, F. Latourte, D. Lemosse, S. Pagano, E. Pagnacco, and F. Pierron. Overview of identification methods of mechanical parameters based on full-field measurements. Exp. Mech., 48(4):381–402, 2008.
4. M. Bertin, F. Hild, and S. Roux. Optimization of a biaxial tensile specimen geometry for the identification of constitutive parameters based upon full field measurements. Strain, 52(4):307–323, 2016.
5. M. Bertin, F. Hild, S. Roux, F. Mathieu, H. Leclerc, and P. Aimedieu. Integrated digital image correlation applied to elastoplastic identification in a biaxial experiment. J. Strain Analysis, 51(2):118–131, 2016.
6. G. Besnard, F. Hild, and S. Roux. "Finite-Element" Displacement Fields Analysis from Digital Images: Application to Portevin-Le Chatelier Bands. Exp. Mech., 46(6):789–803, 2006.

7. G.B. Broggiato. Adaptive image correlation technique for full-field strain measurement. In C. Pappalettere, editor, 12th Int. Conf. Exp. Mech., pages 420–421. McGraw Hill, Lilan (Italy), 2004.
8. J.-Y. Cognard, V. Feuardent, and J.-M. Virely. Optimisation of a structure for biaxial mechanical tests. Integrated Des. Manufact. Mech. Eng., pages 495–504, 1997.
9. G. Del Piero. Constitutive equation and compatibility of the external loads for linear elastic masonry-like materials. Meccanica, 24:150–162, 1989.
10. S. Demmerle and J.P. Boehler. Optimal design of biaxial tensile cruciform specimens. J. Mech. Phys. Solids, 41(1):143–181, 1993.
11. J.E. Dorn. Stress-Strain Rate Relations for Anisotropic Plastic Flow. J. Appl. Phys., 20:15–20, 1949.
12. C.O. Frederick and P.J. Armstrong. A mathematical representation of the multiaxial bauschinger effect. Mat. High Temp., 24(1):1–26, 1966.
13. Y. Hanabusa, H. Takizawa, and T. Kuwabara. Numerical verification of a biaxial tensile test method using a cruciform specimen. J. Mat. Proc. Technol., 213(6):961–970, 2013.
14. F. Hild and S. Roux. Digital Image Correlation: from Displacement Measurement to Identification of Elastic Properties – a Review. Strain, 42(2):69–80, 2006.
15. R. Hill. A theory of the yielding and plastic flow of anisotropic metals. Proc. Royal Soc. London A, 193(1033):281–297, May 1948.
16. R. Hill. Continuum micro-mechanics of elastoplastic polycrystals. J. Mech. Phys. Solids, 13(2):89–101, 1965.
17. ISO. Metallic materials - Tensile testing - Part 1: Method of test at room temperature. International Organization for Standardization, 2011.
18. T. Kuwabara, S. Ikeda, and K. Kuroda. Measurement and analysis of differential work hardening in cold-rolled steel sheet under biaxial tension. J. Mat. Proc. Technol., 80-81:517–523, 1998.
19. W. T. Lankford, S. C. Snyder, and J. A. Bausher. New criteria for predicting the press performance of deep drawing sheets. Trans. ASM, 42:1197–1205, 1950.
20. H. Leclerc, J.N. Périé, S. Roux, and F. Hild. Integrated digital image correlation for the identification of mechanical properties, volume LNCS 5496, pages 161–171. Springer, Berlin, 2009.
21. D. Lecompte, S. Cooreman, S. Coppieters, J. Vantomme, H. Soly, and D. Debruyne. Parameter identification for anisotropic plasticity model using digital image correlation. comparison between uniaxial and bi-axial tensile testing. Europ. J. Comput. Mech., 18:393–418, 2009.
22. J. Lemaitre and J.L. Chaboche. Mechanics of Solid Materials. Cambridge University Press, Cambridge (UK), 1990.
23. A. Leybold-Herbert. Axial-load fatigue tests on 17-7 PH stainless steel under constant-amplitude loading. NASA TN D-439 62 71013, National Aeronautics and Space Administration, Langley Research Center Langley Field, Va (USA), October 1960.
24. O. Mahmood, B. Audoly, and S. Roux. Cracks in tension field theory. 2016. preprint, 2016.
25. F. Mathieu, H. Leclerc, F. Hild, and S. Roux. Estimation of Elastoplastic Parameters via Weighted FEMU and Integrated DIC. Exp. Mech., 55(1):105–119, 2015.
26. M. Poncelet, G. Barbier, B. Raka, S. Courtin, R. Desmorat, J.C. Le-Roux, and L. Vincent. Biaxial high cycle fatigue of a type 304l stainless steel: Cyclic strains and crack initiation detection by digital image correlation. Eur. J. Mech. A/Solids, 29:810–825, 2010.
27. W. Prager. A New Method of Analyzing Stresses and Strains in Work-hardening Plastic Solids. Technical report (Brown University. Division of Applied Mathematics). 1955.
28. J. Réthoré. A fully integrated noise robust strategy for the identification of constitutive laws from digital images. Int. J. Num. Meth. Eng., 84(6):631–660, 2010.
29. S. Schmaltz and K. Willner. Comparison of different biaxial tests for the inverse identification of sheet steel material parameters.

Strain, 50(5):389–403, 2014.

30. S. Soare, J.W. Yoon, O. Cazacu, and F. Barlat. Applications of a Recently Proposed Anisotropic Yield Surface to Sheet Metal Forming, pages 131–149. Springer Berlin, 2007.
31. D. J. Steigmann. Tension field theory. Proc. Royal Soc. London A, 429(1876):141–173, 1990.
32. Y. Sun, J. Pang, C. Wong, and F. Su. Finite-element formulation for a digital image correlation method. Appl. Optics, 44(34):7357–7363, 2005.
33. M.A. Sutton, J.J. Orteu, and H. Schreier. Image correlation for shape, motion and deformation measurements: Basic Concepts, Theory and Applications. Springer, New York, NY (USA), 2009.
34. M. Teaca, I. Charpentier, M. Martiny, and G. Ferron. Identification of sheet metal plastic anisotropy using heterogeneous biaxial tensile tests. Int. J. Mech. Sci., 52(4):572–580, 2010.
35. H.É. Tresca. Mémoire sur l'écoulement des corps solides soumis à de fortes pressions. C.R. Acad. Sci. Paris, 59:754–759, 1864.
36. R von Mises. Mechanik der festen Koerper im plastisch-deformablen Zustand. Nachrichten von der Gesellschaft der Wissenschaften zu Goettingen, Mathematisch-Physikalische Klasse, pages 582–592, 1913.
37. B. Wagne, S. Roux, and F. Hild. Spectral approach to displacement evaluation from image analysis. Eur. Phys. J. AP, 17:247–252, 2002.
38. Y. Yu, M. Wan, X.-D. Wu, and X.-B. Zhou. Design of a cruciform biaxial tensile specimen for limit strain analysis by FEM. J. Mat. Proc. Technol., 123(1):67–70, 2002.

